Research Article

Capacitance and voltage matching between MnO₂ nanoflake cathode and Fe₂O₃ nanoparticle anode for high-performance asymmetric micro-supercapacitors

Zehua Liu[1], Xiaocong Tian[1], Xu Xu[1] (✉), Liang He[1], Mengyu Yan[1], Chunhua Han[1], Yan Li[1], Wei Yang[1], and Liqiang Mai[1,2] (✉)

[1] *State Key Laboratory of Advanced Technology for Materials Synthesis and Processing, Wuhan University of Technology, Wuhan 430070, China*

[2] *Department of Chemistry, University of California, Berkeley, CA 94720, USA*

ABSTRACT

Planar micro-supercapacitors show great potential as the energy storage unit in miniaturized electronic devices. Asymmetric structures have been widely investigated in micro-supercapacitors, and carbon-based materials are commonly applied in the electrodes. To integrate different metal oxides in both electrodes in micro-supercapacitors, the critical challenge is the pairing of different faradic metal oxides. Herein, we propose a strategy of matching the voltage and capacitance of two faradic materials that are fully integrated into one high-performance asymmetric micro-supercapacitor by a facile and controllable fabrication process. The fabricated micro-supercapacitors employ MnO₂ as the positive active material and Fe₂O₃ as the negative active material, respectively. The planar asymmetric micro-supercapacitors possess a high capacitance of 60 F·cm⁻³, a high energy density of 12 mW·h·cm⁻³, and a broad operation voltage range up to 1.2 V.

1 Introduction

The current trend in miniaturized electronic devices and systems, which play significant roles in social developments and daily life, is the increase in demand for microscale power sources [1–3]. Since they can be integrated into chips with other electronic components, microscale energy storage devices are especially important for integrated multifunctional chips and systems [4–6]. The widely used nickel foam and carbon cloth are excellent choices for loading active materials. However, they have considerable mass and size and cannot meet the demands of microchip compatibility. Thus, it is important to develop microscale current collectors with ideal electrode constructions. Micro-supercapacitors (MSCs), one of the most attractive types of energy storage device, rely on ultrathin current collectors, and have shown great potential for

---

Address correspondence to Xu Xu, xuxu@whut.edu.cn; Liqiang Mai, mlq518@whut.edu.cn

application in portable electronics and next-generation electricity systems [7–9]. To realize portable electronic devices with embedded energy-storage devices, it is necessary to integrate MSCs into the device circuit [10]. Therefore, it is advantageous to fabricate planar supercapacitors via lithographic techniques, rather than using conventionally produced vertically stacked supercapacitors. It is becoming increasingly important and urgent to develop MSCs with high energy densities and wide operating voltages in limited spaces, while maintaining high power densities, fast charging/discharging rates, and long cycling lifetimes [11–13].

Aqueous media seem promising because they are cheap and ecologically friendly. In supercapacitor electrolytes, they are characterized by high conductivity and low viscosity compared to organic electrolytes. However, the voltage range of MSCs operating in such electrolytes is thermodynamically limited, because water decomposes at 1.23 V. Recently, asymmetric MSCs (A-MSCs) have gained significant attention. This effective design not only increases the energy density in an aqueous electrolyte, but also reduces the number of series-connected devices required for applications with wide operating voltage ranges [14–16]. Great progress has been made in the design and realization of various A-MSCs [17–19]. However, the commonly employed anodes in previously reported A-MSCs are carbon-based materials that show high conductivities, high stabilities, and low costs [20–22], while the coupling of different metal oxides is rarely studied. Since the total capacitance of A-MSCs is highly dependent on the specific capacitances of the active materials employed for both sides [23], the limited capacitance of carbon-based materials would negatively affect the energy storage capabilities of A-MSCs, despite the inherent high electrical conductivity of the materials. It is possible, but challenging, to integrate two suitable metal oxides into one MSC to maximize the potential window as well as the energy storage capabilities. In conventional pseudocapacitors, MnO_2 has attracted significant interest as a cathodic material because it is low in cost, high in theoretical specific capacitance (1,370 $F \cdot g^{-1}$), naturally abundant, and eco-friendly [24, 25]. Meanwhile, Fe_2O_3 nanomaterials have significant advantages when serving as anodic materials for supercapacitors because they are low-cost,

abundant, and low in toxicity at room temperature [26, 27]. A-MSC electrodes operate reversibly in different potential ranges with different electro-chemical mechanisms, thus increasing the operation voltage range and improving the energy density while maintaining high power density [20]. Therefore, by matching the voltage and capacitance of a MnO_2 cathode and Fe_2O_3 anode, A-MSCs with high electro-chemical performance can be achieved.

In our work, planar A-MSCs are first designed and fabricated, in which MnO_2 and Fe_2O_3 are employed as the cathodic and anodic materials, respectively. During the charging/discharging process, MnO_2 reacts with K^+, and Fe_2O_3 reacts with OH^- in the KOH electrolyte. By matching these two metal oxides, enhanced capacitance and energy density are obtained in the A-MSCs. The as-fabricated A-MSCs operate in the wide voltage window of 1.2 V, show an ultrahigh stack capacitance of 60 $F \cdot cm^{-3}$, specific energy density of 12 $mW \cdot h \cdot cm^{-3}$, and long cycling life of 2,500 cycles. To the best of our knowledge, this is the first report of novel planar A-MSCs based on MnO_2 and Fe_2O_3 nanostructures with the effective matching of voltage and capacitance between these two low-cost metal oxides. The proposed facile and scalable microfabrication process for the integration of these two metal oxides into A-MSCs shows potential for the development of high-performance on-chip micro-energy storage components.

2 Experimental

2.1 Microfabrication of planar MSCs

Figure 1 schematically depicts the microfabrication process for the planar A-MSCs. A Si wafer with a 300-nm-thick SiO_2 layer is employed as the substrate and cleaned by isopropyl alcohol. PR1-9000A photoresist (Futurrex) is uniformly spin-coated on the substrate at 4,000 rpm for 40 s and pre-baked at 100 °C for 15 min. A photolithography process is conducted to obtain interdigital micropatterns and a Cr/Ni layer (5/50 nm) is deposited on the sample as the current collector using a physical vapor deposition (PVD) technique. A lift-off process is conducted with acetone to remove the photoresist; the remaining
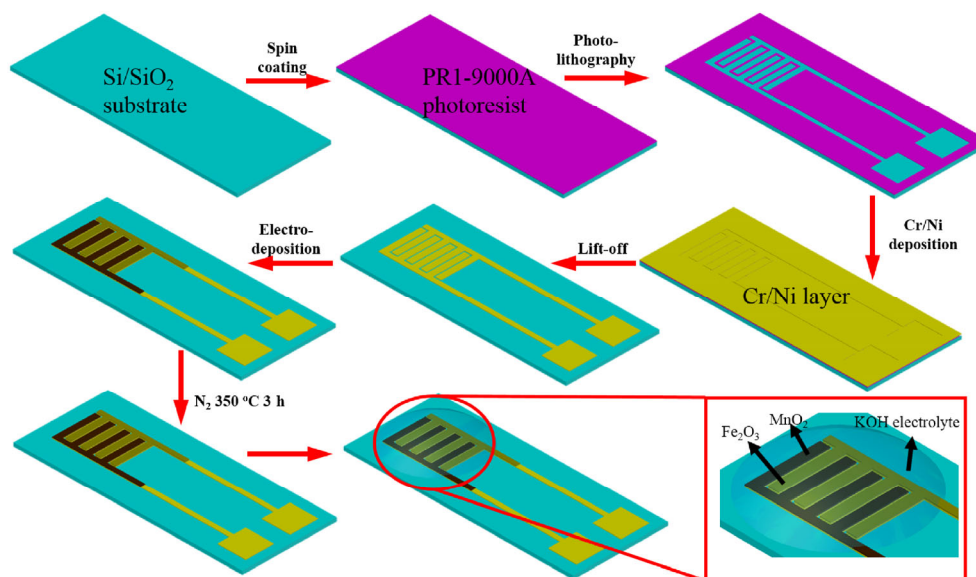
Figure 1 Schematic of the microfabrication process for planar A-MSCs. Firstly, Si/SiO$_2$ substrate is cleaned. Secondly, photoresist is spin-coated on the substrate and interdigital micropatterns are achieved through photolithography. After photolithography, a Cr/Ni layer is deposited on the sample by PVD. Thirdly, the photoresist is removed by a lift-off process. MnO$_2$ nanoflakes and Fe$_2$O$_3$ nanoparticles are then electrochemically deposited on the corresponding interdigital microelectrodes. Finally, 1 M KOH electrolyte is introduced, and the planar A-MSCs are assembled.

photoresist is removed by oxygen plasma treatment at 100 W for 90 s. Afterward, MnO$_2$ nanoflakes and Fe$_2$O$_3$ nanoparticles are electrodeposited on the micropatterned Cr/Ni collector by a three-electrode configuration in which the fabricated microelectrodes, Hg/HgO, and Pt foil are used as the working, reference, and counter electrodes, respectively. For the deposition of MnO$_2$, galvanostatic electrodeposition is performed at a current of 0.05 mA vs. Hg/HgO for 200 s in 25-mM Mn(CH$_3$COO)$_2$ and 25-mM CH$_3$COONa aqueous solution. For Fe$_2$O$_3$ nanoparticles, galvanostatic electrodeposition is performed at a current of –0.15 mA vs. Hg/HgO for 100 s in 25-mM Fe(NO$_3$)$_3$·9H$_2$O and 25-mM NaNO$_3$ aqueous solution. After electrodeposition, the A-MSCs are annealed at 350 $^\circ$C under N$_2$ for 3 h to convert the anode precursor to Fe$_2$O$_3$ [28]. Finally, 1 M KOH is dropped onto the interdigital microelectrodes as the electrolyte. All reagents are analytical-grade and used as received without further purification.

MnO$_2$ microelectrode-based symmetric MSCs (M-MSCs) and Fe$_2$O$_3$ microelectrode-based symmetric MSCs (F-MSCs) are fabricated using the same processes mentioned above. 1 M KOH is again employed as the electrolyte in these devices.

2.2 Characterization of planar MSCs

The morphologies and elemental compositions of the planar A-MSCs, M-MSCs, and F-MSCs were characterized using a field-emission scanning electron microscope (FE-SEM, JEOL JSM-7100F) at an acceleration voltage of 20 kV. X-ray diffraction (XRD, D8 Discover X-ray diffractometer, Bruker) was applied to identify the crystal phases of the specimens using a non-monochromatic Co Kα X-ray source (λ = 1.7902 Å). The thicknesses of the as-fabricated microelectrodes were measured by a stylus surface profiler (Bruker DektakTX) and the chemical bonds of the as-synthesized active materials were investigated using X-ray photoelectron spectroscopy (XPS VG Multilab 2000). Raman spectra were collected by a Renishaw RM-1000 laser Raman microscopy system. Cyclic voltammetry (CV) curves, galvanostatic charge–discharge (GCD) curves, and cycle life curves were recorded by an electrochemical workstation (Autolab PGSTAT302N). The planar MSCs were placed in a sealed probe station chamber (Desert Cryogenics Probe Station TTPX) during the electrochemical testing. All measurements were performed at room temperature.

3   Results and discussion

In comparison with the conventional sandwiched structure that is incompatible with integrated circuits (ICs), microfabrication methods have enabled the integration of MSCs into interdigital planar devices. Consequently, we take advantage of microfabrication methods to integrate current collectors into miniaturized electronic devices and systems. Among the deposition methods for metal oxide electrodes, electrodeposition has demonstrated multiple benefits such as facile mass control, excellent conductivity, and precise control during the oxidation process, which is applied to deposit active microelectrodes in this research [29].

The morphology of the A-MSC with eight planar interdigital microelectrodes (four MnO_2 cathodes and four Fe_2O_3 anodes) is shown in Fig. 2(a). Only the right side of the electrode, which is slightly brighter than the left side, is covered by Fe_2O_3. It can be clearly observed that the interdigital microelectrodes have well-defined and defect-free micropatterns, and no short circuits between the microelectrodes are detected. The micropatterned Cr/Ni current collector is well covered by the as-deposited materials and the

photoresist between the electrodes is completely removed. As shown in Fig. 2(b), where the top side of the microelectrode is coated with Fe_2O_3, the width of each interdigital microelectrode is 400 μm and the interspace is 100 μm. Figures 2(c) and 2(d) show high-magnification SEM images of the MnO_2 nanoflakes, which are uniformly distributed over the micro-electrode surface. Energy-dispersive X-ray spectroscopy (EDX) analysis (Fig. 2(g)) shows a homogeneous distribution of Mn and O elements. The high-magnification SEM images (Figs. 2(e) and 2(f)) exhibit the uniform coating of the right interdigital microelectrode with Fe_2O_3 nanoparticles. The EDX analysis (Fig. 2(h)) also shows a homogeneous distribution of Fe and O elements. The crystallographic phases of the as-synthesized materials are evaluated by XRD, as shown in Fig. S1 in the Electronic Supplementary Material (ESM), which indicates their amorphous natures.

Figure 3 shows the phase compositions of the microelectrodes in the planar A-MSCs. Raman spectroscopy is applied to investigate the detailed bonding configurations of MnO_2 and Fe_2O_3 in Figs. 3(a) and 3(c), respectively. The fundamental Raman
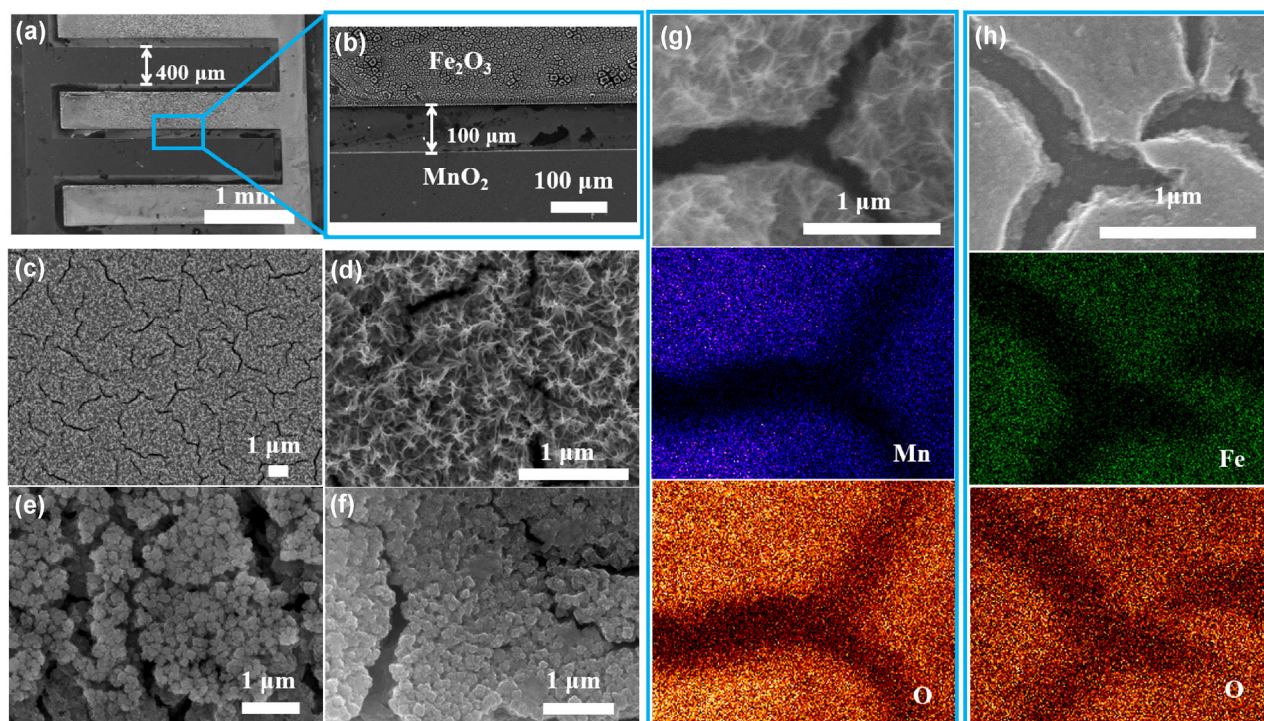
Figure 2   Morphologies and elemental compositions of planar MSCs. SEM images of A-MSCs ((a) and (b)), M-MSCs ((c) and (d)), and F-MSCs ((e) and (f)). EDX mappings of MnO_2 (g) and Fe_2O_3 (h).
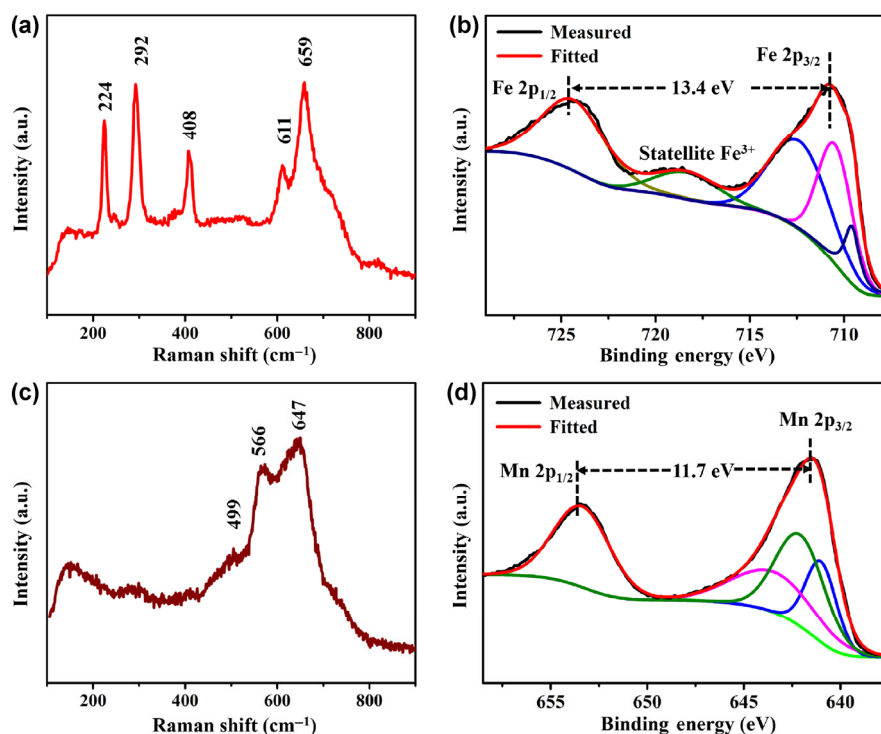
Figure 3 Phase compositions of planar MSCs. (a) Raman spectrum of Fe_2O_3 nanoparticles. (b) XPS spectrum of Fe 2p in Fe_2O_3 nanoparticles. (c) Raman spectrum of MnO_2 nanoflakes. (d) XPS spectrum of Mn 2p in MnO_2 nanoflakes.

scattering peaks of Fe_2O_3 nanoparticles are observed at 224 cm^{-1} (A_{1g} mode), and 292, 408, 611, and 659 cm^{-1} (E_g modes) [30]. The Raman spectrum represented in Fig. 3(c) verifies the presence of MnO_2 nanoflakes by their characteristic Raman peaks at 499, 566, and 647 cm^{-1}, which are in agreement with previously reported results [31, 32]. To further characterize the chemical components and valence states of the microelectrodes in the A-MSCs, XPS analysis is further conducted. The XPS spectrum of Fe 2p is shown in Fig. 3(b). Three distinct peaks occur at the binding energies of 709.5, 710.4, and 712.3 eV for Fe $2p_{3/2}$, and one peak at 724.2 eV for Fe $2p_{1/2}$, with a shake-up satellite at 718.6 eV in the Fe 2p core-level spectrum, which corresponds well with the literature values of Fe_2O_3 [33]. Figure S2(a) in the ESM shows the O 1s spectrum of the Fe_2O_3 nanoparticles, which is decomposed into two main constituent peaks corresponding to Fe–O–Fe bonds (529.6 and 531.2 eV) [34, 35]. The Mn 2p spectrum in Fig. 3(d) shows the Mn $2p_{3/2}$ multiplet (640.9, 642.1, and 643.3 eV) and a Mn $2p_{1/2}$ peak (653.4 eV), which is in accordance with previous results [36]. The energy separation (11.7 eV) between

the Mn $2p_{1/2}$ and Mn $2p_{3/2}$ peaks suggests that the dominant Mn species is Mn(IV) in the as-deposited MnO_2 nanoflakes [21]. The O 1s core-level spectrum was also used to confirm the oxidation state of Mn (Fig. S2(b) in the ESM). Figure S2(b) in the ESM shows that the spectrum can be fitted with three main peaks at 529.9, 531.5, and 532.6 eV, related to Mn–O–Mn, Mn–O–H, and H–O–H bonds, respectively [37–39], which are attributed to the absorption of O_2 and water molecules on the MnO_2 nanoflake surfaces. All these results confirmed the expected electrodeposition of MnO_2 and Fe_2O_3.

Electrochemical measurements of A-MSCs, M-MSCs, and F-MSCs were conducted in a two-electrode system using 1 M KOH as the aqueous electrolyte. To determine the potential window of the A-MSCs, electrochemical studies of the MnO_2 and Fe_2O_3 were conducted in a three-electrode configuration with Hg/HgO and Pt foil as the reference electrode and the counter electrode, respectively (shown in Fig. S3 in the ESM). The optimized potential window of Fe_2O_3 is from −1.1 to −0.5 V (Fig. S3(a) in the ESM), while the potential window of MnO_2 is from −0.5 to 0.1 V

(Fig. S3(b) in the ESM) in 1 M KOH. By taking advantage of the different potential windows of MnO_2 and Fe_2O_3 (Fig. S3(c) in the ESM), it is expected that the operating potential of our A-MSCs can be extended to 1.2 V. As we know, this potential is greater than most reported results, such as carbon/Ni/NiO MSCs (0–0.6 V) [9], carbon/carbon nanotube (CNT) MSCs (0–0.8 V) [12], MnO_2/carbon MSCs (0–1 V) [16], Si/TiC/carbon MSCs (−0.6–0.2 V) [40], multi-walled CNT/V_2O_5 MSCs (0–0.8 V) [41], and $Ti_3C_2T_x$/graphene MSCs (0–0.8 V) [42]. For the development of A-MSCs, matching the capacitances between the positive and negative electrodes is critical for achieving the best possible electrochemical performance. Considering that the medium deposition process contributes to balancing the performance between the capacitances of MnO_2 and Fe_2O_3, the capacitances of MnO_2 and Fe_2O_3 were used to obtain the parameters for their electrodeposition processes by the following calculations. The charge stored in an electrode is expressed as Eq. (1) [2]

$$q = m C_{sp} \Delta V \qquad (1)$$

where m is the mass loading of electrode (in g), C_{sp} is the specific capacitance (in F·g^{-1}), and ΔV is the operation potential window (in V). In order to match the capacitances of the cathodic and anodic electrodes, we should suppose the equalization of charges on the two electrodes of the A-MSC, i.e., $q_+ = q_-$ is required. According to Eq. (1), we obtain the follow equation

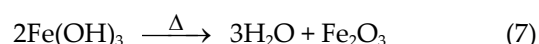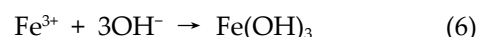$$\frac{m_+}{m_-} = \frac{C_{sp-} \Delta V_-}{C_{sp+} \Delta V_+} \qquad (2)$$

The C_{sp} of MnO_2 and Fe_2O_3 in the three-electrode configuration can be calculated from the CV curves using the following equation

$$C_{sp} = \frac{\int i \, dV}{2s \times \Delta V \times m} \qquad (3)$$

where i is the measured current (in A) and s is the scan rate (in V·s^{-1}). The C_{sp} values of MnO_2 and Fe_2O_3 are 120 and 150 F·g^{-1} at 20 mV·s^{-1}, respectively (Fig. S3(d) in the ESM). Meanwhile, MnO_2 is deposited onto Cr/Ni via galvanostatic electrodeposition. The half-reaction on the interdigital microelectrodes may be expressed as follows [43]

$$Mn(CH_3COO)_2 + 2H_2O \rightarrow MnO_2 + 2CH_3COOH + 2H^+ + 2e^- \qquad (4)$$
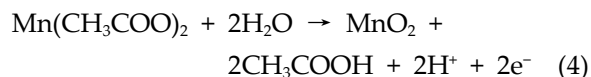
The deposition of Fe_2O_3 also consumes nitrate ions at the electrode surface to generate hydroxide ions (see Eq. (5)). Fe^{3+} ions react with locally generated hydroxide ions to form metallic hydroxide deposits on the electrode surfaces according to Eq. (6) [44]. $Fe(OH)_3$ can be converted to Fe_2O_3 by annealing (Eq. (7)) [28].

$$NO_3^- + 7H_2O + 8e^- \rightarrow NH_4^+ + 10OH^- \qquad (5)$$

$$Fe^{3+} + 3OH^- \rightarrow Fe(OH)_3 \qquad (6)$$

$$2Fe(OH)_3 \xrightarrow{\Delta} 3H_2O + Fe_2O_3 \qquad (7)$$

The mass of active materials (m in g) can be calculated by Eq. (8)

$$It = n \times \frac{m}{M} \times F \qquad (8)$$

where I (in A) is the current during galvanostatic electrodeposition, t (in s) is the galvanostatic electrodeposition time, n is the gains and losses of electrons in the two half-reactions (2 for MnO_2 and 4.8 for Fe_2O_3), M (in g·mol^{-1}) is the molar mass of the active materials, and F (in C·mol^{-1}) is the Faraday constant. Therefore, the mass ratio of the active materials can be expressed as follow

$$\frac{m_+}{m_-} = \frac{I_+ t_+ M_+ n_-}{I_- t_- M_- n_+} \qquad (9)$$

Accordingly, the follow equation can be obtained from Eqs. (2) and (9)

$$\frac{I_+ t_+}{I_- t_-} = \frac{C_{sp-} \Delta V_- M_- n_+}{C_{sp+} \Delta V_+ M_+ n_-} \qquad (10)$$

Based on the specific capacitance values and potential windows of MnO_2 and Fe_2O_3, the optimal $I_+ t_+/I_- t_-$ should be 2/3. Hence, capacitance matching can be achieved by controlling the current and time during the electrodeposition. The CV curves of A-MSCs over a potential window of 0–1.2 V were measured at various scan rates from 20 to 20,000 mV·s^{-1}, while the CV measurements of M-MSCs and F-MSCs were conducted in the potential range of 0–0.6 V. Figure 4(a) shows the CV curves of the A-MSCs
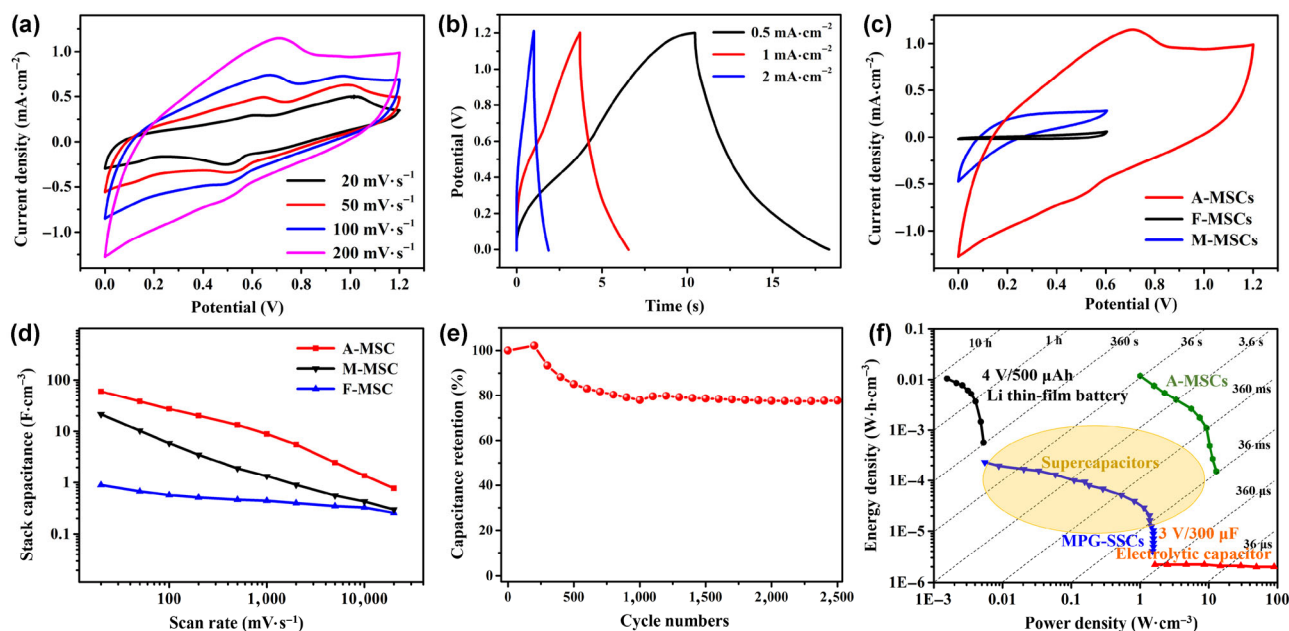
Figure 4 Electrochemical performance of planar MSCs. (a) CV curves of A-MSCs at various scan rates in 1 M KOH with the potential window from 0 to 1.2 V. (b) GCD curves of A-MSCs (0–1.2 V) at various current densities. (c) CV curves of A-MSCs, M-MSCs, and F-MSCs at the scan rate of 200 mV·s⁻¹ in 1 M KOH. (d) Stack capacitance evolution of planar MSCs at different scan rates ranging from 20 to 20,000 mV·s⁻¹. (e) Cycling stability of A-MSCs at a scan rate of 2,000 mV·s⁻¹ in 1 M KOH electrolyte. (f) Ragone plot of the specific volumetric energy density vs. power density for A-MSCs in comparison with typical batteries, electrolytic capacitors, supercapacitors, and MPG-SSCs.

with various scan rates from 20 to 200 mV·s⁻¹, while Figs. S4(a) and S4(b) in the ESM show the CV curves of the M-MSCs and F-MSCs, respectively. Regardless of the scan rate, the CV curves of the A-MSCs are nearly rectangular with small redox peaks, indicating the occurrence of a Faraday redox reaction. With increasing scan rates, the cathodic peak shifts to a more positive position and the anodic peak to a more negative one, which can be attributed to the increase of the internal diffusion resistance.

The electrochemical performance of the A-MSCs was further investigated by GCD at different current densities of 0.5–2 mA·cm⁻² (Fig. 4(b)). The GCD curves exhibit predominantly asymmetric natures, indicating that the A-MSCs have good electrochemical characteristics with reversible redox reactions. The voltage drop related to the overall internal resistance value can be estimated from the GCD curves. Figure S5 in the ESM shows the voltage drop of the A-MSCs at various current densities. The slope of the voltage drop is 0.15, which indicates a minor overall internal resistance drop. Figure 4(c) shows the CV curves at a

scan rate of 200 mV·s⁻¹. Obviously, the current of the A-MSCs is larger than those of the M-MSCs and F-MSCs, representing a solution available by the coupling of different metal oxides as active materials to realize higher capacitances, energy densities, and potential window widths.

Recently, it has been shown that the stack capacitance has greater realistic significance than the gravimetric capacitance, because the mass loading of active materials is very low in microdevices [45]. Thus, the stack capacitance provides a more accurate estimate of the real performance of a supercapacitor than gravimetric values [6, 19]. Therefore, the stack capacitances (C_v in F·cm⁻³) of the MSCs are used as parameters to characterize their performances. The stack capacitances are estimated from the CV curves at different scan rates by the following equation

$$C_{sp} = \frac{\int i \, dV}{2s \times \Delta V \times S} \quad (11)$$

where i is the measured current (in A), s is the scan rate (in V·s⁻¹), ΔV is the operation potential window

(in V), and S is the total volume (in cm^3) of the device including the cathode, anode, current collector, and electrolyte. Here, the average thicknesses are measured as 522 and 1,398 nm for the MnO_2 and Fe_2O_3 microelectrodes (including the current collectors), respectively. The measured thicknesses of the individual MnO_2 and Fe_2O_3 microelectrodes are listed in Table S1 in the ESM. Considering the different thicknesses of the A-MSCs, M-MSCs, and F-MSCs, the thicknesses of the A-MSCs and F-MSCs are estimated as 1,398 nm, while that of the M-MSCs is 522 nm by calculation. The stack capacitances of A-MSCs, M-MSCs, and F-MSCs at different scan rates are shown in Fig. 4(d). Noticeably, the A-MSCs show a much higher stack capacitance of 60 $F \cdot cm^{-3}$ compared to those of the M-MSCs (20 $F \cdot cm^{-3}$) or F-MSCs (0.9 $F \cdot cm^{-3}$) at 20 $mV \cdot s^{-1}$. This capacitance is higher than most reported results, such as those of reduced graphene oxide (rGO) MSCs (3.1 $F \cdot cm^{-3}$) [6], $Ti_3C_2T_x$/graphene MSCs (40 $F \cdot cm^{-3}$) [42], laser rGO MSCs (3.05 $F \cdot cm^{-3}$) [46], and graphene/CNT MSCs (1.08 $F \cdot cm^{-3}$) [47].

The stack capacitance C_v is also calculated from the GCD curves according to Eq. (12)

$$C_v = \frac{I \times \Delta t}{S \times \Delta V} \qquad (12)$$

where I is the discharge current (in A), Δt is the discharge time (in s), S is the total volume (in cm^3) of the MSC including the cathode, anode, current collector, and electrolyte, and ΔV is the potential window (in V). The stack capacitances of A-MSCs, M-MSCs, and F-MSCs at different current densities are shown in Fig. S6 in the ESM. The A-MSCs show the highest stack capacitance of 24 $F \cdot cm^{-3}$ at a current density of 0.5 $mA \cdot cm^{-2}$, while the M-MSCs and F-MSCs deliver 14 and 1 $F \cdot cm^{-3}$ at 1 $mA \cdot cm^{-2}$, respectively. The cycling life is also an important parameter of MSCs for practical applications. In this study, we evaluated the cycling life by repeating CV tests for 2,500 cycles at 2,000 $mV \cdot s^{-1}$. Figure 4(e) shows that the A-MSCs have a long cycling life retaining 80% of the initial specific capacitance after 2,500 cycles.

To characterize the overall performance of the A-MSCs, the specific energy densities (E, in $W \cdot h \cdot cm^{-3}$) and average specific power densities (P_{av}, in $W \cdot cm^{-3}$) of the A-MSCs were calculated by Eqs. (13) and (14)

$$E = \frac{C_v \times (\Delta V)^2}{7200} \qquad (13)$$

$$P_{av} = \frac{E}{\Delta t} \times 3600 \qquad (14)$$

where C_v is the stack capacitance (in $F \cdot cm^{-3}$) calculated by the CV curves, ΔV is the operation potential window (in V) and Δt is the discharge time (in s). Figure 4(f) demonstrates the Ragone plots of E and P_{av} of the A-MSCs. With high specific capacitances (60 $F \cdot cm^{-3}$) and broad operating voltage ranges (1.2 V), the A-MSCs deliver a maximum energy density of 12 $mW \cdot h \cdot cm^{-3}$ at a power density of 1 $W \cdot cm^{-3}$ and 35 $\mu W \cdot h \cdot cm^{-3}$ at 14.8 $W \cdot cm^{-3}$. For comparison, the results of previous studies are also included in the Ragone plot: the commercial high-energy Li thin-film battery (4 V/500 mA·h) [48], the high-power aluminum electrolytic capacitor (3 V/300 mF) [49], and the methane (CH_4)-plasma reduction graphene sandwich-supercapacitors (MPG-SSCs) [50]. Noticeably, the A-MSCs show the highest energy density and a relatively high power density among these results. For comparison with the A-MSCs, E and P_{av} for the M-MSCs and F-MSCs were also calculated by Eqs. (13) and (14), as shown in Fig. S7 in the ESM.

It is widely known that two main mechanisms dominate in pseudocapacitive metal oxides: the adsorption/desorption and reduction/oxidation processes. The mechanism of MnO_2 for charge storage is as follows ($M^+ = H^+, Li^+, Na^+, K^+$) [20, 51]

$$MnO_2 + M^+ + e^- \rightleftharpoons MnOOM \qquad (15)$$

The capacitance of Fe_2O_3 is mainly derived from the pseudocapacitive charging/discharging based on the following reversible redox reaction [52]

$$Fe_2O_3 + OH^- \rightleftharpoons Fe_2O_3OH + e^- \qquad (16)$$

From the above mechanisms, we speculate a mechanism for the electrochemical behavior of the A-MSCs as follows (regarded as synergistic effects of the combination of MnO_2 and Fe_2O_3, shown in Fig. 5). During the charging, Fe_2O_3 reacts with OH^- in the KOH electrolyte to form Fe_2O_3OH. In the meantime, MnO_2 is transformed into MnOOK by reacting with K^+ in the KOH electrolyte. During discharge, with the
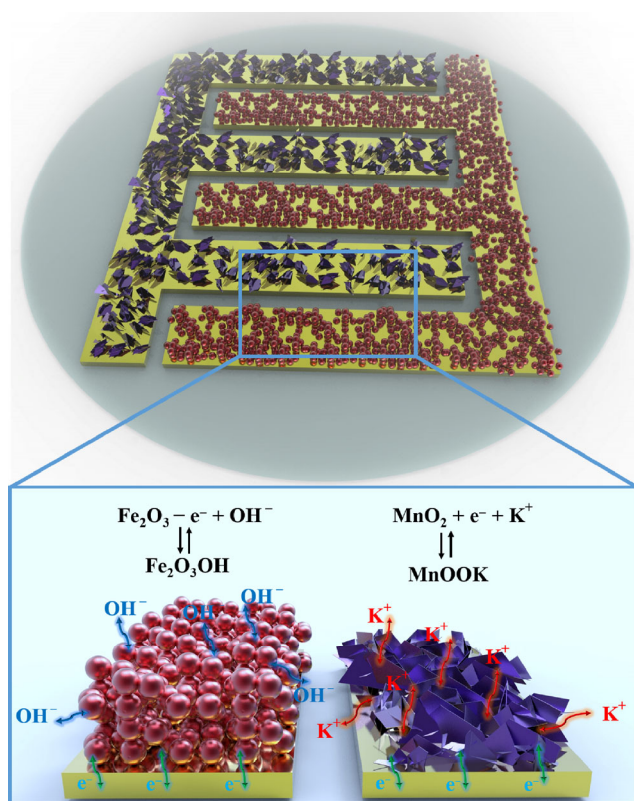
Figure 5   Schematic of storage mechanism of A-MSCs.

occurrence of the reverse reactions, MnOOK and Fe_2O_3OH are transformed into MnO_2 and Fe_2O_3 by releasing OH^- anions and K^+ cations into the KOH electrolyte, respectively. By using the complementary potential windows of the anode and cathode, the performance of the A-MSCs is enhanced. Since the capacitances of the cathode and anode are of the same order, the maximum energy density of the A-MSCs is enhanced.

4   Conclusions

In this work, we presented the design and assembly of planar A-MSCs with MnO_2 nanoflake cathode, Fe_2O_3 nanoparticle anode, and alkaline aqueous electrolyte for the first time. We also proposed a strategy to match their capacitances by optimizing the current and time of the electrodeposition of the cathode and anode materials. The as-fabricated A-MSCs have outstanding capacitive performance and long cycling lifetime within a voltage range of 1.2 V and deliver the high energy density of 12 mW·h·cm^{-3}. Furthermore, the

mechanism of their high performance is discussed. The synergistic effect between MnO_2 and Fe_2O_3 may be responsible for the enhanced performance of the A-MSCs. This facile and controllable integration of low-cost electrode materials and compatible micro-fabrication technologies gives the proposed A-MSCs great potential for practical applications in future high-performance microscale power sources.

Acknowledgements

References

[1]   Kudo, A.; Miseki, Y. Heterogeneous photocatalyst materials for water splitting. *Chem. Soc. Rev.* **2009**, *38*, 253–278.

[2]   Achilleos, D. S.; Hatton, T. A. Surface design and engineering of hierarchical hybrid nanostructures for asymmetric supercapacitors with improved electrochemical performance. *J. Colloid Interface Sci.* **2015**, *447*, 282–301.

[3]   Mai, L. Q.; Tian, X. C.; Xu, X.; Chang, L.; Xu, L. Nanowire electrodes for electrochemical energy storage devices. *Chem. Rev.* **2014**, *114*, 11828–11862.

[4]   Beidaghi, M.; Wang, C. L. Micro-supercapacitors based on interdigital electrodes of reduced graphene oxide and carbon nanotube composites with ultrahigh power handling performance. *Adv. Funct. Mater.* **2012**, *22*, 4501–4510.

[5] Tian, X. C.; Xiao, B.; Xu, X.; Xu, L.; Liu, Z. H.; Wang, Z. Y.; Yan, M. Y.; Wei, Q. L.; Mai, L. Q. Vertically stacked holey graphene/polyaniline heterostructures with enhanced energy storage for on-chip micro-supercapacitors. *Nano Res.* **2016**, *9*, 1012–1021.

[6] El-Kady, M. F.; Kaner, R. B. Scalable fabrication of high-power graphene micro-supercapacitors for flexible and on-chip energy storage. *Nat. Commun.* **2013**, *4*, 1475.

[7] Ma, X. Y.; Luo, W.; Yan, M. Y.; He, L.; Mai, L. Q. *In situ* characterization of electrochemical processes in one dimensional nanomaterials for energy storages devices. *Nano Energy* **2016**, *24*, 165–188.

[8] Xu, Y. F.; Schwab, M. G.; Strudwick, A. J.; Hennig, I.; Feng, X. L.; Wu, Z. S.; Müllen, K. Screen-printable thin film supercapacitor device utilizing graphene/polyaniline inks. *Adv. Energy Mater.* **2013**, *3*, 1035–1040.

[9] Yin, C.; He, L.; Wang, Y. F.; Liu, Z. H.; Zhang, G. B.; Zhao, K. N.; Tang, C. J.; Yan, M. Y.; Han, Y. L.; Mai, L. Q. Pyrolyzed carbon with embedded NiO/Ni nanospheres for applications in microelectrodes. *RSC Adv.* **2016**, *6*, 43436–43441.

[10] Lee, G.; Kim, D.; Yun, J.; Ko, Y.; Cho, J.; Ha, J. S. High-performance all-solid-state flexible micro supercapacitor arrays with layer-by-layer assembled MWNT/MnO$_x$ nano-composite electrodes. *Nanoscale* **2014**, *6*, 9655–9664.

[11] Mai, L. Q.; Xu, X.; Han, C. H.; Luo, Y. Z.; Xu, L.; Wu, Y. A.; Zhao, Y. L. Rational synthesis of silver vanadium oxides/polyaniline triaxial nanowires with enhanced electro-chemical property. *Nano Lett.* **2011**, *11*, 4992–4996.

[12] Simon, P.; Gogotsi, Y. Materials for electrochemical capacitors. *Nat. Mater.* **2008**, *7*, 845–854.

[13] Yang, Y. J.; He, L.; Tang, C. J.; Hu, P.; Hong, X. F.; Yan, M. Y.; Dong, Y. X.; Tian, X. C.; Wei, Q. L.; Mai, L. Q. Improved conductivity and capacitance of interdigital carbon microelectrodes through integration with carbon nanotubes for micro-supercapacitors. *Nano Res.* **2016**, *9*, 2510–2519.

[14] Xu, H. H.; Hu, X. L.; Yang, H. L.; Sun, Y. M.; Hu, C. C.; Huang, Y. H. Flexible asymmetric micro-supercapacitors based on Bi$_2$O$_3$ and MnO$_2$ nanoflowers: Larger areal mass promises higher energy density. *Adv. Energy Mater.* **2015**, *5*, 1401882.

[15] Zhou, C.; Zhang, Y. W.; Li, Y. Y.; Liu, J. P. Construction of high-capacitance 3D CoO@polypyrrole nanowire array electrode for aqueous asymmetric supercapacitor. *Nano Lett.* **2013**, *13*, 2078–2085.

[16] Long, J. W.; Bélanger, D.; Brousse, T.; Sugimoto, W.; Sassin, M. B.; Crosnier, O. Asymmetric electrochemical capacitors-stretching the limits of aqueous electrolytes. *MRS Bull.* **2011**, *36*, 513–522.

[17] Shen, C. W.; Wang, X. H.; Li, S. W.; Wang, J. G.; Zhang, W. F.; Kang, F. Y. A high-energy-density micro super-capacitor of asymmetric MnO$_2$-carbon configuration by using micro-fabrication technologies. *J. Power Sources* **2013**, *234*, 302–309.

[18] Yu, D. S.; Goh, K.; Zhang, Q.; Wei, L.; Wang, H.; Jiang, W. C.; Chen, Y. Controlled functionalization of carbonaceous fibers for asymmetric solid-state micro-supercapacitors with high volumetric energy density. *Adv. Mater.* **2014**, *26*, 6790–6797.

[19] Liu, W. W.; Yan, X. B.; Chen, J. T.; Feng, Y. Q.; Xue, Q. J. Novel and high-performance asymmetric micro-supercapacitors based on graphene quantum dots and polyaniline nanofibers. *Nanoscale* **2013**, *5*, 6053–6062.

[20] Yan, J.; Wang, Q.; Wei, T.; Fan, Z. J. Recent advances in design and fabrication of electrochemical supercapacitors with high energy densities. *Adv. Energy Mater.* **2014**, *4*, 1300816.

[21] Wang, Q.; Yan, J.; Fan, Z. J. Carbon materials for high volumetric performance supercapacitors: Design, progress, challenges and opportunities. *Energy Environ. Sci.* **2016**, *9*, 729–762.

[22] Bonaccorso, F.; Colombo, L.; Yu, G. H.; Stoller, M.; Tozzini, V.; Ferrari, A. C.; Ruoff, R. S.; Pellegrini, V. Graphene, related two-dimensional crystals, and hybrid systems for energy conversion and storage. *Science* **2015**, *347*, 1246501.

[23] Jeong, H. M.; Lee, J. W.; Shin, W. H.; Choi, Y. J.; Shin, H. J.; Kang, J. K.; Choi, J. W. Nitrogen-doped graphene for high-performance ultracapacitors and the importance of nitrogen-doped sites at basal planes. *Nano Lett.* **2011**, *11*, 2472–2477.

[24] Toupin, M.; Brousse, T.; Bélanger, D. Charge storage mechanism of MnO$_2$ electrode used in aqueous electro-chemical capacitor. *Chem. Mater.* **2004**, *16*, 3184–3190.

[25] Yang, P. H.; Ding, Y.; Lin, Z. Y.; Chen, Z. W.; Li, Y. Z.; Qiang, P. F.; Ebrahimi, M.; Mai, W. J.; Wong, C. P.; Wang, Z. L. Low-cost high-performance solid-state asymmetric supercapacitors based on MnO$_2$ nanowires and Fe$_2$O$_3$ nanotubes. *Nano Lett.* **2014**, *14*, 731–736.

[26] Qu, Q. T.; Yang, S. B.; Feng, X. L. 2D sandwich-like sheets of iron oxide grown on graphene as high energy anode material for supercapacitors. *Adv. Mater.* **2011**, *23*, 5574–5580.

[27] Wu, M. S.; Ou, Y. H.; Lin, Y. P. Electrodeposition of iron oxide nanorods on carbon nanofiber scaffolds as an anode material for lithium-ion batteries. *Electrochim. Acta* **2010**, *55*, 3240–3244.

[28] Lokhande, B. J.; Ambare, R. C.; Mane, R. S.; Bharadwaj, S. R. Concentration-dependent electrochemical supercapacitive performance of Fe$_2$O$_3$. *Curr. Appl. Phys.* **2013**, *13*, 985–989.

[29] Zhang, C.; Xiao, J.; Qian, L. H.; Yuan, S. L.; Wang, S.; Lei, P. X. Planar integration of flexible micro-supercapacitors with ultrafast charge and discharge based on interdigital nanoporous gold electrodes on a chip. *J. Mater. Chem. A* **2016**, *4*, 9502–9510.

[30] de Faria, D. L. A.; Silva, S. V.; de Oliveira, M. T. Raman microspectroscopy of some iron oxides and oxyhydroxides. *J. Raman Spectrosc.* **1997**, *28*, 873–878.

[31] Julien, C.; Massot, M.; Rangan, S.; Lemal, M.; Guyomard, D. Study of structural defects in γ-MnO$_2$ by Raman spectroscopy. *J. Raman Spectrosc.* **2002**, *33*, 223–228.

[32] Duay, J.; Sherrill, S. A.; Gui, Z.; Gillette, E.; Lee, S. B. Self-limiting electrodeposition of hierarchical MnO$_2$ and M(OH)$_2$/MnO$_2$ nanofibril/nanowires: Mechanism and supercapacitor properties. *ACS Nano* **2013**, *7*, 1200–1214.

[33] Grosvenor, A. P.; Kobe, B. A.; Biesinger, M. C.; McIntyre, N. S. Investigation of multiplet splitting of Fe 2p XPS spectra and bonding in iron compounds. *Surf. Interface Anal.* **2004**, *36*, 1564–1574.

[34] Nefedov, V. I.; Salyn, Y. V.; Leonhardt, G.; Scheibe, R. A comparison of different spectrometers and charge corrections used in X-ray photoelectron spectroscopy. *J. Electron Spectrosc. Relat. Phenom.* **1977**, *10*, 121–124.

[35] Lee, Y. S.; Kim, H. T.; Yoo, K. O. Effect of ferric oxide on the high-temperature removal of hydrogen sulfide over ZnO-Fe$_2$O$_3$ mixed metal oxide sorbent. *Ind. Eng. Chem. Res.* **1995**, *34*, 1181–1188.

[36] Nesbitt, H. W.; Banerjee, D. Interpretation of XPS Mn(2p) spectra of Mn oxyhydroxides and constraints on the mechanism of MnO$_2$ precipitation. *Am. Mineral.* **1998**, *83*, 305–315.

[37] Chigane, M.; Ishikawa, M. Manganese oxide thin film preparation by potentiostatic electrolyses and electrochromism. *J. Electrochem. Soc.* **2000**, *147*, 2246–2251.

[38] Di Castro, V.; Polzonetti, G.; Contini, G.; Cozza, C.; Paponetti, B. XPS Study of MnO$_2$ minerals treated by bioleaching. *Surf. Interface Anal.* **1990**, *16*, 571–574.

[39] Stranick, M. A. MnO$_2$ by XPS. *Surf. Sci. Spectra* **1999**, *6*, 31–38.

[40] Huang, P.; Lethien, C.; Pinaud, S.; Brousse, K.; Laloo, R.; Turq, V.; Respaud, M.; Demortière, A.; Daffos, B.; Taberna, P. L. et al. On-chip and freestanding elastic carbon films for micro-supercapacitors. *Science* **2016**, *351*, 691–695.

[41] Kim, D.; Yun, J.; Lee, G.; Ha, J. S. Fabrication of high performance flexible micro-supercapacitor arrays with hybrid electrodes of MWNT/V$_2$O$_5$ nanowires integrated with a SnO$_2$ nanowire UV sensor. *Nanoscale* **2014**, *6*, 12034–12041.

[42] Kong, L. B.; Bai, R. J.; Luo, Y. C.; Kang, L. A comparative study of potentiostatic and potentiodynamic method in the synthesis of MnO$_2$ films for electrochemical capacitors. *Adv. Mater. Res.* **2011**, *239–242*, 501–505.

[43] Li, H. Y.; Hou, Y.; Wang, F. X.; Lohe, M. R.; Zhuang, X. D.; Niu, L.; Feng, X. L. Flexible all-solid-state supercapacitors with high volumetric capacitances boosted by solution processable MXene and electrochemically exfoliated graphene. *Adv. Energy Mater.* **2017**, *7*, 1601847.

[44] Lu, X. Y.; Zhao, C. Electrodeposition of hierarchically structured three-dimensional nickel-iron electrodes for efficient oxygen evolution at high current densities. *Nat. Commun.* **2015**, *6*, 6616.

[45] Gogotsi, Y.; Simon, P. True performance metrics in electro-chemical energy storage. *Science* **2011**, *334*, 917–918.

[46] Gao, W.; Singh, N.; Song, L.; Liu, Z.; Reddy, A. L. M.; Ci, L. J.; Vajtai, R.; Zhang, Q.; Wei, B. Q.; Ajayan, P. M. Direct laser writing of micro-supercapacitors on hydrated graphite oxide films. *Nat. Nanotechnol.* **2011**, *6*, 496–500.

[47] Lin, J.; Zhang, C. G.; Yan, Z.; Zhu, Y.; Peng, Z. W.; Hauge, R. H.; Natelson, D.; Tour, J. M. 3-Dimensional graphene carbon nanotube carpet-based microsupercapacitors with high electrochemical performance. *Nano Lett.* **2013**, *13*, 72–78.

[48] Pech, D.; Brunet, M.; Durou, H.; Huang, P. H.; Mochalin, V.; Gogotsi, Y.; Taberna, P. L.; Simon, P. Ultrahigh-power micrometre-sized supercapacitors based on onion-like carbon. *Nat. Nanotechnol.* **2010**, *5*, 651–654.

[49] El-Kady, M. F.; Strong, V.; Dubin, S.; Kaner, R. B. Laser scribing of high-performance and flexible graphene-based electrochemical capacitors. *Science* **2012**, *335*, 1326–1330.

[50] Wu, Z. S.; Parvez, K.; Feng, X. L.; Müllen, K. Graphene-based in-plane micro-supercapacitors with high power and energy densities. *Nat. Commun.* **2013**, *4*, 2487.

[51] Mai, L. Q.; Dong, F.; Xu, X.; Luo, Y. Z.; An, Q. Y.; Zhao, Y. L.; Pan, J.; Yang, J. N. Cucumber-like V$_2$O$_5$/poly(3,4-ethylenedioxythiophene)&MnO$_2$ nanowires with enhanced electrochemical cyclability. *Nano Lett.* **2013**, *13*, 740–745.

[52] Zhu, M. Y.; Wang, Y.; Meng, D. H.; Qin, X. Z.; Diao, G. W. Hydrothermal synthesis of hematite nanoparticles and their electrochemical properties. *J. Phys. Chem. C* **2012**, *116*, 16276–16285.